Applied Mathematical Modelling 38 (2014) 4249–4261

Contents lists available at ScienceDirect

Applied Mathematical Modelling

journal homepage: www.elsevier.com/locate/apm

Modelling bubble rise and interaction with a glass surface ☆

Rogerio Manica [a,*], Maurice H.W. Hendrix [b,c], Raghvendra Gupta [a,d], Evert Klaseboer [a], Claus-Dieter Ohl [c], Derek Y.C. Chan [a,e,f]

[a] Institute of High Performance Computing, 1, Fusionopolis Way, Singapore 138632, Singapore
[b] Physics of Fluids, University of Twente, P.O. Box 217, 7500 AE Enschede, The Netherlands
[c] School of Physical and Mathematical Sciences, Nanyang Technological University, Singapore 637371, Singapore
[d] Department of Chemical Engineering, Birla Institute of Technology & Science, Pilani, K K Birla Goa Campus, Zuaringar, 403 726 Goa, India
[e] Department of Mathematics and Statistics, The University of Melbourne, VIC 3010, Australia
[f] Faculty of Life and Social Science, Swinburne University of Technology, Hawthorn 3122, Australia

A R T I C L E I N F O

Article history:
Received 27 June 2013
Received in revised form 21 November 2013
Accepted 21 March 2014
Available online 3 April 2014

Keywords:
Multiscale
Microhydrodynamics
Bubble impact
Immobile interfacial boundary condition
Lubrication

A B S T R A C T

A theoretical model has been developed to analyse bubble rise in water and subsequent impact and bounce against a horizontal glass plate. The multiscale nature of the problem, where the bubble size is on the millimetre range and the film drainage process happens on the micrometre to nanometre scale requires the combined use of different modelling techniques. On the macro scale we solve the full Navier–Stokes equations in cylindrical coordinates to model bubble rise whereas modelling film drainage on the micro scale is based on lubrication theory because the film Reynolds number becomes much smaller than unity. Quantitative predictions of this model are compared with experimental data obtained using synchronised high-speed cameras. Video recording of bubble rise and bounce trajectories are combined with interferometry data to deduce the position and time-dependent thickness of the thin water film trapped between the deformed bubble and the glass plate. Bubble rise velocity indicated that the boundary condition at the bubble surface was tangentially immobile. Quantitative comparisons are presented for bubbles of different size to quantify similarities and differences.

1. Introduction

Interactions of soft materials such as drops and bubbles with solid surfaces occur in a wide variety of fields ranging from the manufacture of pharmaceuticals and detergents to water purification and mineral extraction. Modelling and numerical simulations of such systems present challenges because particle motions, interfacial interactions and deformations occur on different length scales. Identifying the bubble interface and its deformation and movement can be done using numerical techniques such as the volume of fluid (VOF) or level-set methods. When a bubble is very close to a solid surface or when two bubbles are very close to each other such techniques require very fine grids and the computational time can become unreasonably large. On the other hand, the use of lubrication theory to model the last stages of thin film drainage can be used if the local Reynolds number of the system is smaller than unity. However, such descriptions must be consistent with the large scale description of the centre of mass motion.

☆ This article belongs to the Special Issue: *Topical Issues drawn from CFD2012 on CFD in the Minerals and Process Industries*.

* Corresponding author. Tel.: +65 64191275; fax: +65 64630200.
E-mail address: manicar@ihpc.a-star.edu.sg (R. Manica).

http://dx.doi.org/10.1016/j.apm.2014.03.039
0307-904X/

Nomenclature

C_d	drag coefficient
d	diameter of the bubble (m)
F_{buoy}	buoyancy force (N)
F_{drag}	drag force (N)
g	gravitational acceleration (m/s^2)
H	initial separation (m)
H_o	typical vertical length scale (m)
$h_o(t)$	film thickness at the centre of interaction (m)
$h_m(t)$	minimum film thickness (m)
$h(r,t)$	film thickness (m)
n	refractive index of water
p	pressure (Pa)
r	radial coordinate (m)
r_{max}	length of computational domain (m)
R	radius of the bubble (m)
R_L	Laplace radius (m)
Re	global Reynolds number
Re_f	film Reynolds number
t	time (s)
$\mathbf{u}$	velocity vector (m/s)
u	radial velocity (m/s)
v	vertical velocity (m/s)
$U(t)$	maximum velocity of the water in the film (m/s)
$V_{CM}(t)$	velocity of centre of mass of the bubble (m/s)
$V(r,t)$	velocity of the bubble surface (m/s)
V_T	approach velocity (m/s)
V_o	typical vertical velocity scale (m/s)
z	vertical coordinate (m)

Greek symbols

σ	interfacial tension (N/m)
ρ	water density (kg/m^3)
μ	water viscosity (Pa s)
λ	wavelength of the laser (m)
Π	disjoining pressure (Pa)

The behaviour of bubbles rising in water under buoyancy has been an active area of research. Terminal velocity data for bubbles of various sizes from different sources have been collated by Clift et al. [1]. Bubbles rising in ultra clean water attain larger velocities that correspond to a mobile (stress free) boundary condition at the bubble surface whereas the presence of contaminants renders the interface to be immobile, obeying the same no-slip boundary condition as that at a solid surface, and results in lower terminal velocities. Bubbles that are partially covered by surfactants or contaminants have intermediate terminal velocities. Exposure of the water to the atmosphere is enough for environmental impurities to contaminate the water over time and change the boundary condition at the bubble surface [2].

Studies on the effect of different surfactants at relatively low concentrations in water found a decrease in terminal velocity of a rising bubble as the surfactant concentration was increased until the velocity reached a constant value [3,4]. Works by Levich [5] and Cuenot et al. [6] indicate that at sufficiently low surfactant concentrations, bubble motion can cause a non-uniform surface distribution of surfactants, where the top or leading portion of a rising bubble remains clean while the surfactants are convected to the bottom, trailing part of the bubble surface. A simple model known as the "stagnant cap model" in which the surfactant-covered boundary is represented as an immobile boundary and surfactant-free surface is modelled as a mobile or stress free boundary can be used to calculate the bubble terminal velocity for different coverage ratios. This model has been solved analytically in the Stokes flow regime [7]. To test the boundary condition that should be applied at the bubble surface we employ ANSYS Fluent to compute terminal velocities under mobile and immobile boundary conditions assuming the bubble to remain spherical, as observed experimentally.

When a bubble collides with a surface, a multiscale problem arises as the separation between the bubble and the surface becomes much smaller than the bubble radius. Observing the small scale microhydrodynamics phenomena of film drainage between the bubble and the surface required different experimental techniques. Most experimental investigations of rising bubbles that collide with a horizontal planar surface were restricted to side view recordings that report deformations in the shape of the bubble and possible bounce trajectories [8–11], but corresponding information about the drainage of the thin film were seldom reported for the same experiments. Interferometry had been used to observe film deformation and drainage, but experimental results were restricted to small deformations and low velocities [12–15]. Those results were modelled using lubrication theory. Improvements of high-speed cameras now allow the study of much faster bubble-surface collisions by capturing the evolution of interference fringes [16,17]. The use of synchronized high-speed cameras to observe phenomena in different length scales has gained popularity, especially for studying drops impacting on flat surfaces in air [18–20] and for quantifying the effects of the Leidenfrost vapour on the splash behaviour of a drop on a hot surface [21,22]. These experiments complement data on the bounce of soap bubbles falling against a water surface [23].

In this work we use modelling and numerical simulations to analyse the experimental data of Hendrix et al. [16] on the interaction and bounce of millimetre-size bubbles rising in water under gravity against a flat horizontal glass surface. The deionised water we used contained trace amounts of impurities and the bubble behaved as immobile interface during rise and interaction with the glass surface.

The manuscript is organised as follows. Description of the problem and the general theory are presented in Section 2. The bubble rise stage (macro scale) is discussed in Section 3. The micro scale, where lubrication theory is derived based on scaling of the problem, is presented in Section 4. Numerical simulations that combined the centre of mass motion with lubrication theory to describe the drainage process all the way to bubble adhesion are compared to the experimental data in Section 5. Finally, the main findings of this work as well as discussions are summarised in Section 6.

2. Theory of rising and bouncing bubbles

In this work we model the experimental data of Hendrix et al. [16]. Details on the experiment and experimental results can be found in that reference. Here we focus on the modelling and comparisons with those experiments. Comparisons will be shown for two typical bubbles of different radii (R = 385 μm and R = 630 μm) among 10 bubbles that were analysed. The small sizes of these bubbles ensure straight vertical rise of the bubbles and axisymmetric deformation resulting from interaction with the glass plate.

A schematic of the experimental system is shown in Fig. 1. A bubble of radius R rises under buoyancy before impacting a glass surface. Two synchronized high speed cameras capture the bubble rise and impact (macro scale) and simultaneously a second camera captures the interference fringes during thin film drainage (micro scale). The fringes can be converted to separations, h using Bragg's equation. For a fringe of order m: $h = m\,\lambda/(2n)$, where λ = 532 nm is the wavelength of the laser and n = 1.33 is the refractive index of water. Parameters of our system are: air/water interfacial tension, σ = 72 mN/m, viscosity of water, μ = 1 mPa s and density of water, ρ = 1000 kg/m^3.

Assuming that the continuous phase is a Newtonian fluid, the rise and impact of the bubble can be modelled by the continuity and Navier–Stokes equations written as:

$$\nabla \cdot \mathbf{u} = 0, \tag{1}$$

$$\rho\left(\frac{\partial \mathbf{u}}{\partial t} + \mathbf{u} \cdot \nabla \mathbf{u}\right) = -\nabla p + \mu \nabla^2 \mathbf{u}, \tag{2}$$

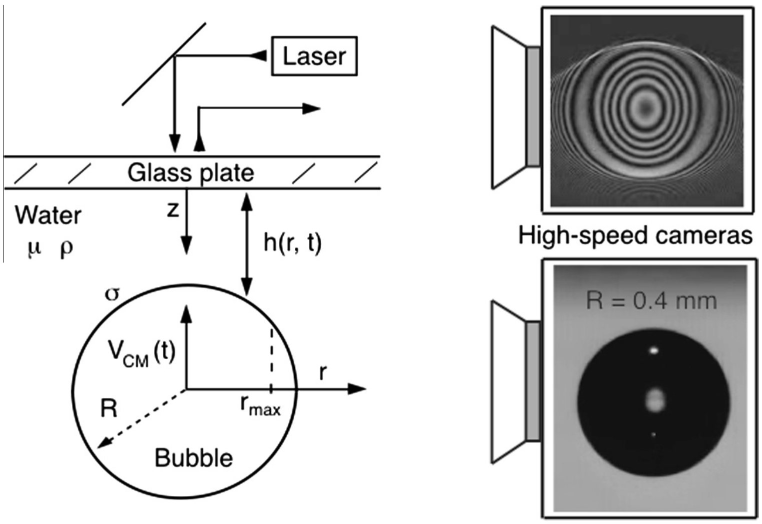

Fig. 1. A bubble of radius R rises with centre of mass velocity $V_{CM}(t)$ against a glass plate in water. The bubble deformation is axisymmetric and is described in terms of the film thickness between the bubble and the plate, $h(r,t)$ with the radial coordinate in the range $r = 0$ to $r = r_{max}$, with $r_{max} < R$. A high-speed camera captures the movement and shape of the rising bubble (bottom right image) and a synchronised second camera records the evolution of the interference fringe pattern formed by the water film trapped between the bubble and the glass surface (top right image).

where $\mathbf{u} = (u, v)$ is the velocity field and p the pressure. Since our problem is axisymmetric we write the continuity and Navier–Stokes equations in cylindrical form

$$\frac{1}{r}\frac{\partial}{\partial r}(ru) + \frac{\partial v}{\partial z} = 0, \tag{3}$$

$$\rho\left(\frac{\partial u}{\partial t} + u\frac{\partial u}{\partial r} + v\frac{\partial u}{\partial z}\right) = -\frac{\partial p}{\partial r} + \mu\left(\frac{1}{r}\frac{\partial}{\partial r}\left[r\frac{\partial u}{\partial r}\right] + \frac{\partial^2 u}{\partial z^2} - \frac{u}{r^2}\right), \tag{4}$$

$$\rho\left(\frac{\partial v}{\partial t} + u\frac{\partial v}{\partial r} + v\frac{\partial v}{\partial z}\right) = -\frac{\partial p}{\partial z} + \mu\left(\frac{1}{r}\frac{\partial}{\partial r}\left[r\frac{\partial v}{\partial r}\right] + \frac{\partial^2 v}{\partial z^2}\right). \tag{5}$$

For our modelling, we determine the boundary conditions at the air–water interface by examining the variation of experimental terminal velocities, V_T of bubbles with radius R between 0.35 mm and 0.75 mm.

3. Macro scale modelling

The terminal velocity V_T of a rising bubble can be used as an indicator of the boundary condition – tangentially immobile (no slip) or tangentially mobile (zero shear stress), that holds on the bubble interface. In the experimental data of Hendrix et al. [16], the global Reynolds numbers based on the terminal velocity, $Re = 2R\,\rho V_T/\mu$ are in the range 60–230 whereby the flow field is steady, laminar and axisymmetric and the bubble shape remain spherical. We performed CFD simulations using ANSYS Fluent to calculate terminal velocity of spherical bubbles for both immobile (no-slip) and mobile (zero stress) boundary conditions at the bubble interface. The bubble is taken to be stationary and the velocity in the far field is taken to be uniform. The terminal velocity for a given bubble size is determined by varying the flow velocity until the drag force becomes equal to the buoyancy force.

The simulations were performed following the guidelines outlined in Magnaudet et al. [24] using a cylindrical computational domain as shown in Fig. 2. A uniform velocity was specified at the inlet whereas an outflow boundary condition that specifies zero diffusion flux for all flow variables was applied at the outlet. The far field boundary is treated as a stress-free wall, i.e. zero radial velocity and zero gradient of axial velocity. The computational mesh was sufficiently refined near the bubble interface (first element near the wall was $0.0018R$) and the mesh size increased on moving away from the bubble. The bubble interface had 50 elements on its semi-circular circumference. A grid refinement study was conducted to ensure that the results were independent of the mesh size and the final mesh used for the simulations consisted of 50,000 elements.

The highest Reynolds number in our CFD simulations for the tangentially immobile (no-slip) boundary was 205. Nakamura [25] and Jones and Clarke [26] have shown that the flow remains axisymmetric and steady up to Reynolds numbers of 210 and 270, respectively. Therefore, the assumption of steady and axisymmetric flow in our CFD simulations is deemed valid. For the case of a stress-free bubble interface, the highest value of the Reynolds number presented here is 316 and the flow was always observed to remain attached to the bubble interface.

By treating the bubbles as a sphere of radius R, the buoyancy force (neglecting the density of gas)

$$F_{\text{buoy}} = \frac{4\pi}{3}\rho R^3 g \tag{6}$$

is balanced by the steady state hydrodynamic drag force

$$F_{\text{drag}} = \frac{1}{2}\rho V_T^2 (\pi R^2) C_d, \tag{7}$$

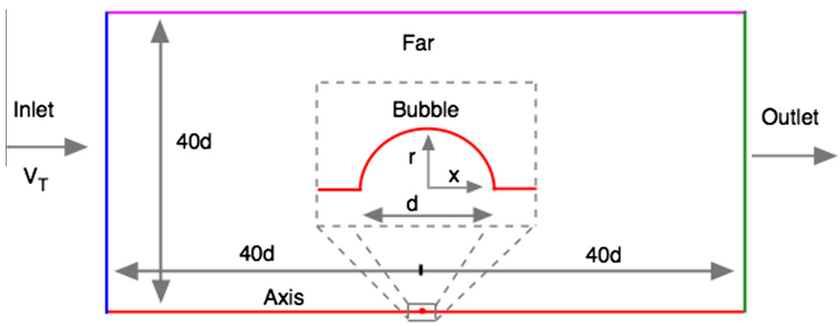

Fig. 2. A schematic of the axisymmetric computational domain in which the dimensions are given in terms of the bubble diameter, $d = 2R$.

where the drag coefficient C_d is a function of the Reynolds number, Re, and g is the acceleration due to gravity. For the immobile (no-slip) boundary condition at the bubble interface, we also compare our results with the empirical Schiller–Naumann formula [1] for C_d that is valid for $Re < 800$:

$$C_d = \frac{24}{\mathrm{Re}}(1 + 0.15\mathrm{Re}^{0.687}). \tag{8}$$

Thus the terminal velocity can also be determined empirically as a function of bubble radius from Eqs. (6)–(8).

In Fig. 3 we show the terminal velocities measured in the experiments of Hendrix et al. [16] (open squares) and compare them with those obtained from the Schiller–Naumann formula, Eqs. (6)–(8), (solid line) and CFD simulations (filled triangles) using the immobile boundary condition at the bubble interface. The excellent agreement of the experimentally obtained terminal velocities with the Schiller–Naumann formula as well as no-slip CFD simulations indicates that the immobile boundary condition should be appropriate.

Terminal velocities measured by Duineveld [27] for deformable bubbles in ultra pure water, where the stress-free boundary condition holds, are plotted together with those obtained from numerical simulations using the boundary element method (BEM) that allowed for bubble deformation [28] (dashed line) and CFD simulations for non-deforming spheres (open triangles). Analytical results of Moore [29] for a spherical bubble (dotted line) as well as ellipsoidal bubble (dash-dot line) [30] derived for stress-free bubble interface are also plotted. The terminal velocities obtained from the CFD simulations for spherical bubbles agree well with the analytical results of Moore for spherical bubbles, but are not in agreement with the experimental data of [16]. On the other hand, the analytical results for elliptical bubbles [30] are in close agreement with the experiment of Duineveld [27].

Streamlines obtained from CFD simulations for stress free (Fig. 3(b)) and immobile boundary condition (Fig. 3(c)) at $Re = 100$ are given for comparison. For the stress-free boundary condition, the flow remains attached to the bubble whereas in the case of the tangentially immobile boundary condition, the flow separates from the bubble boundary at about 120° from the upstream stagnation point and a vortex develops on the downstream side of the bubble. As there is significant shear stress on the bubble in the case of the immobile boundary condition, the total drag – a combination of form and skin friction drag – increases and the bubble rises with a lower terminal velocity.

4. Micro scale modelling

Our system is characterised by two different length scales: the macro scale of the bubble and the micro scale of thin film drainage of water trapped between the rising bubble and the glass plate. In Fig. 4 we present a schematic of the micro scale, where the variables for the calculations are defined.

In our system the film Reynolds number, $Re_f\,(=\rho H_o V_o/\mu)$ becomes small when the bubble is close to the glass plate due to small separation H_o ($\sim$10 μm) and low velocity of the bubble surface, V_o ($\sim$1 mm/s) and therefore, inertial effects can be neglected in the film. The axisymmetric Navier–Stokes and continuity equations (3)–(5) can be simplified into the lubrication form (see Appendix A for full derivation)

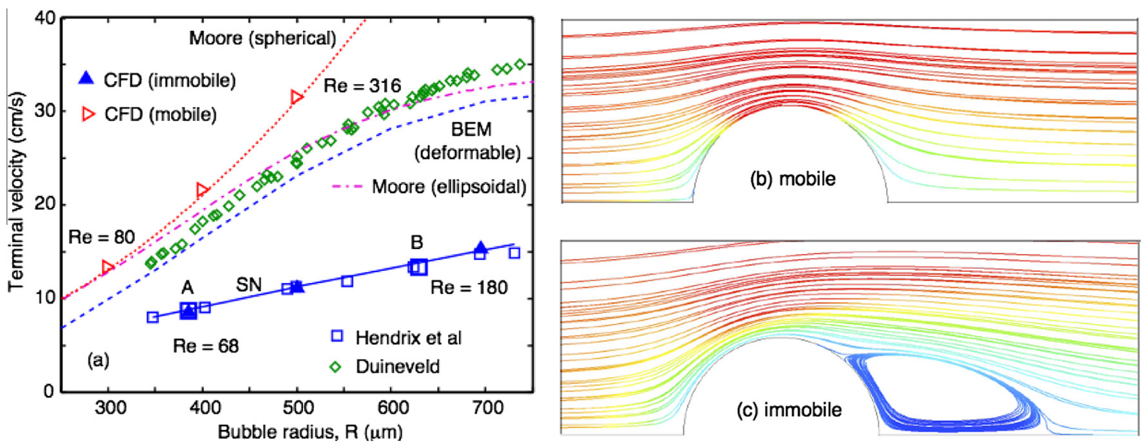

Fig. 3. (a) Terminal velocities for CFD simulations of axisymmetric flow around a spherical bubble with no-slip boundary condition (filled triangles) compared to that predicted using the Schiller–Naumann formula (solid line) and to experiments (squares) [16]. Results for the stress-free boundary condition obtained from the boundary element method (BEM) that allows for bubble deformation [28] (dashed line) and CFD calculations for non-deforming spherical bubbles (open triangles) are compared to analytical results for spherical bubbles [29] (dotted line), ellipsoidal bubbles [30] (dash-dot line) and also to experiment for bubbles in clean water [27] (open diamonds). The data points marked "A" and "B" correspond to radii 385 μm and 630 μm, respectively and will be analysed further in the next section. Streamlines of CFD numerical simulations for (b) mobile and (c) immobile boundary conditions for $Re = 100$.

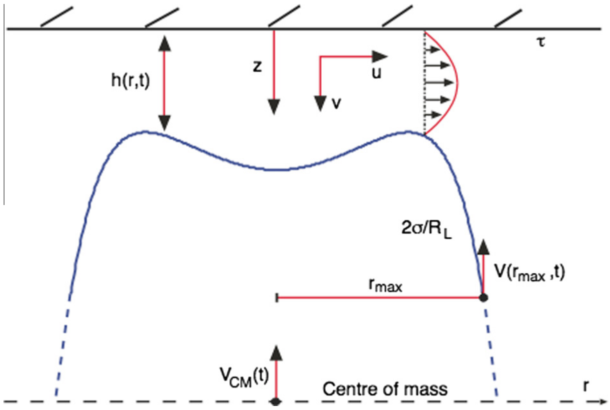

Fig. 4. Schematic of the micro scale where a nearly flat thin film of water of thickness $h(r,t)$ is trapped between the rising bubble and the glass plate. A dimple region is indicated. The velocity profile in this thin film is parabolic.

$$\frac{\partial p}{\partial r} = \mu \frac{\partial^2 u}{\partial z^2}, \tag{9}$$

$$\frac{\partial p}{\partial z} = 0, \tag{10}$$

$$\frac{\partial v}{\partial z} = -\frac{1}{r}\frac{\partial (ru)}{\partial r}, \tag{11}$$

where u and v are the velocity components in the r and z directions (see Fig. 4).

At the glass plate, the no-slip boundary conditions implies $u = v = 0$ at $z = 0$. Assuming that the immobile boundary condition holds at the bubble interface, the tangential component of velocity must be zero, that means, $u = 0$ at $z = h(r,t)$. This assumption is based on experimental observations presented earlier [16]. The classical condition for clean water systems assumes the mobile boundary condition at the bubble surface. The bubble approaches the glass surface with velocity $V(r,t)$. Therefore, $v = -V(r,t) = \partial h/\partial t$ at $z = h(r,t)$. As the pressure p does not depend on z according to Eq. (10), Eq. (9) can be integrated twice with respect to z, and applying boundary conditions for u gives

$$u = \frac{1}{2\mu}(z^2 - hz)\frac{\partial p}{\partial r}. \tag{12}$$

The maximum radial velocity of the film is at $z = h/2$, midway between the glass and the bubble surface, with the value

$$U(r,t) = -\frac{h(r,t)^2}{8\mu}\frac{\partial p}{\partial r}. \tag{13}$$

The viscous shear stress at the glass surface ($z = 0$) and at the bubble ($z = h$) can be calculated from [31]

$$\tau = \mu \frac{\partial u}{\partial z}\bigg|_{z=0} = -\frac{h}{2}\frac{\partial p}{\partial r}, \tag{14a}$$

$$\tau = -\mu \frac{\partial u}{\partial z}\bigg|_{z=h} = -\frac{h}{2}\frac{\partial p}{\partial r}. \tag{14b}$$

Substituting u from Eq. (12) into the continuity equation (Eq. (11)) and integrating from $z = 0$ to h we obtain the equation for the evolution of the thickness of the water film between the bubble and the glass surface [32]

$$\frac{\partial h}{\partial t} = \frac{c}{12\mu r}\frac{\partial}{\partial r}\left(r\, h^3 \frac{\partial p}{\partial r}\right), \tag{15}$$

where $c = 1$ for an immobile boundary condition at the bubble surface: $u = 0$ at $z = h$, used in this work. The mobile boundary condition: $\tau = 0$ at the bubble surface $z = h$ would give $c = 4$.

The characteristic deformation time of the air/water interface in our experiment is small compared to the typical experimental time. Therefore it is justified to assume that the deformation of the bubble in the thin film takes place under quasi-equilibrium conditions and is governed by the familiar Young–Laplace equation that relates the mean curvature of a fluid interface to the pressure difference across the interface. In addition to the Laplace pressure ($2\sigma/R_L$) between the two sides of the curved interface, there are two additional contributions to the pressure difference, namely, the disjoining pressure

Π on the interface and the hydrodynamic pressure p, due to the drainage of the aqueous film trapped between the bubble and the surface. Thus if the bubble deformations are axially symmetric as observed experimentally, the pressure p obeys the augmented Young–Laplace equation of the form [33]

$$\sigma(\kappa_1+\kappa_2)\equiv\frac{\sigma}{r}\frac{\partial}{\partial r}\left(\frac{r\,h_r}{\left(1+h_r^2\right)^{1/2}}\right)=\frac{2\sigma}{R_L}-\Pi-p, \tag{16}$$

where ($h_r\equiv\partial h/\partial r$), R_L is the Laplace radius ($R_L\sim R$) and σ is the interfacial tension. Furthermore, when the film is flat we have $\partial h/\partial r\ll 1$so that

$$\frac{\sigma}{r}\frac{\partial}{\partial r}\left(r\frac{\partial h}{\partial r}\right)=\frac{2\sigma}{R_L}-\Pi(h)-p. \tag{17}$$

Note that $\Pi(h)$ is only important when the separation becomes small (<0.1 μm) just before bubble adhesion and therefore can be neglected in this work.

The initial condition must be consistent with Eq. (17) so that it produces a zero film pressure. This requirement is satisfied by a parabolic surface for the bubble, which is the local approximation to a sphere with radius R, as the initial condition

$$h(r,0)=H+\frac{r^2}{2R}, \tag{18}$$

where H is the initial separation and time t = 0 is taken at a position where the bubble is still rising at constant velocity and the deformation due to the presence of the glass surface is negligible.

We also need four boundary conditions. Due to symmetry:

$$\frac{\partial p}{\partial r}=0=\frac{\partial h}{\partial r}\quad\text{at } r=0. \tag{15}$$

For the far-field boundary condition the pressure decays as $1/r^4$ [34] so that

$$r\frac{\partial p}{\partial r}+4p=0\quad\text{at } r=r_{\max}. \tag{16}$$

The last boundary condition assumes

$$\frac{\partial h}{\partial t}=-V(r_{\max},t)\quad\text{at } r=r_{\max} \tag{17}$$

the same condition used in [31]. In our simulations $V(r_{\max},t)$ is taken to be the velocity of the bubble at $r_{\max}$ = 0.7R from the experimental data. This velocity is close to the velocity of the centre of mass of the bubble (see Fig. 4(b)). Another possibility is to calculate the velocity of the centre of mass through a balance of forces [35,36].

Numerical simulations are performed using ODE solver *ode15s* in Matlab. The system of equations is solved from r = 0 to r = $r_{\max}$ = 0.7R (see Figs. 1 and 4) with a grid spacing of 2 μm.

5. Bubble impact with the glass surface

In Fig. 5(a) we present the experimental velocity of the centre of mass for two bubbles with different radii (R = 385 μm and R = 630 μm). As the bubble approaches and interacts with the surface, the velocity decreases, and eventually becomes negative when the bubble bounces and the centre of mass starts to move away from the glass surface. The bubble velocity then oscillates before stopping after about 50 ms trapping a film of water between the bubble and the glass surface. This film drains for about 200 ms before the film breaks and the bubble adheres to the glass surface.

In Fig. 5(b) we compare experimental measurement of the velocity of the centre of mass as well as at r = 0.7R which is used as a boundary condition in our simulations. The velocities are obtained by tracking the position of the entire bubble surface in the video using Matlab. Although there is good concordance between the two velocities, using the velocity at $r_{\max}$ in the boundary condition provides better agreement between model and experiment in the film drainage stage.

In what follows, we present comparisons between experiments and numerical simulations using lubrication theory for these two bubbles sizes. The shape of the interference fringe patterns of bubble and the glass surface indicate that the interaction remains axisymmetric. Moreover, these bubbles never fully detach from the glass after the first contact so this allows absolute determination of the film thickness based on the point of film rupture.

In Fig. 6 we show the comparison between thickness of the film between bubble and glass surface as obtained from lubrication theory (solid lines) and experiments (symbols) during the first encounter between the bubble and the glass surface. The agreement is excellent in both the timing and spatial position without any adjustable parameters in the model. As the bubble approaches the glass surface, the pressure in the film rises (see Fig. 8) and when it becomes larger than the internal pressure ($2\sigma/R$) of the bubble, it causes inversion of the bubble curvature to form the so-called dimple. Note that this process lasts for only a few milliseconds.

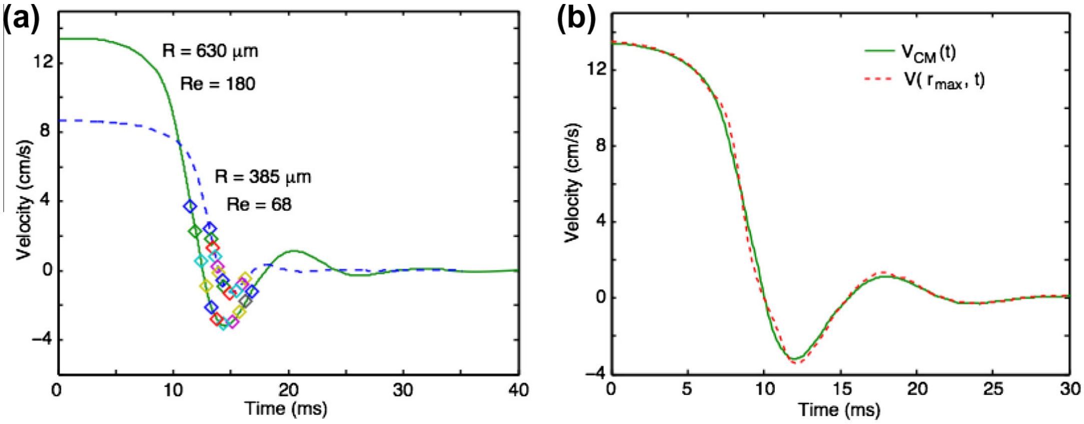

Fig. 5. (a) Experimental velocity of the centre of mass as a function of time for two bubbles of different radii: $R = 385\ \mu m$ (dashed line) and $R = 630\ \mu m$ (solid line). Diamonds correspond to the time instants for which the bubble profiles are compared in Fig. 6. (b) Velocity at the centre of mass and at $r = 0.7R = r_{max}$ for $R = 630\ \mu m$.

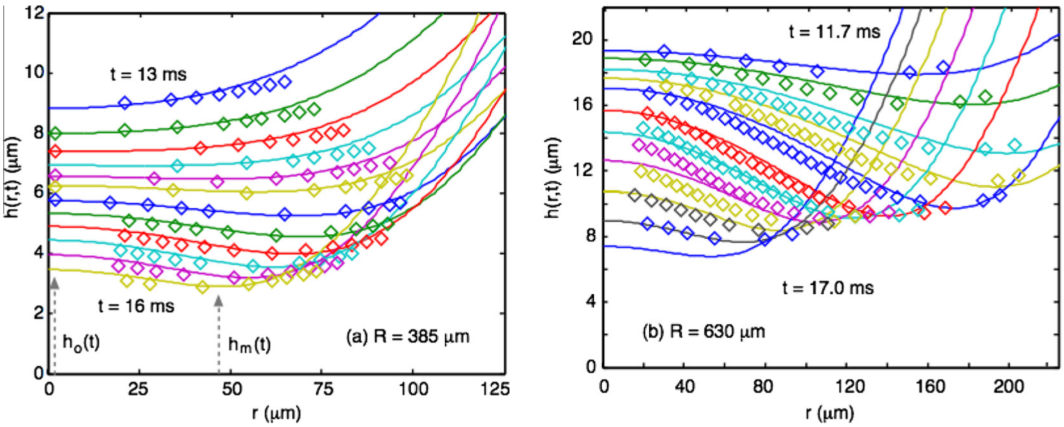

Fig. 6. Comparison between lubrication theory (solid lines) and experimental data (symbols) for the spatiotemporal evolution of the bubble shape during the first encounter with the glass corresponding to selected time instants in Fig. 5(a): (a) $R = 385\ \mu m$, (b) $R = 630\ \mu m$. The domain size was taken to be $r_{max} = 270\ \mu m$ for the bubble with radius $R = 385\ \mu m$ and $r_{max} = 450\ \mu m$ for the bubble with radius $R = 630\ \mu m$.

From the results obtained using lubrication theory, we see that even as the outside of the bubble retreats, the inner part of film is still thinning and the local interface approaches the glass surface until the bubble eventually bounces. This "suction effect" is similar to the one attributed to have caused the coalescence of two bubbles in the Atomic Force Microscope (AFM) experiments of Vakarelski et al. [37] while being separated from each other.

Results for thin film drainage using lubrication theory for the position at the centre $h_o(t)$ (solid line) as well as the position where the film is the thinnest $h_m(t)$ (dashed line) are presented in Fig. 7. The excellent agreement between experiments (symbols) and lubrication theory all the way to bubble attachment indicates that lubrication is the main contribution during the interaction process once the film becomes thin enough. Dimple formation (when $h_o(t)$ becomes greater than $h_m(t)$) happens at a larger thickness ($\sim$19 μm) for the larger bubble compared to the small one ($\sim$6 μm). Notice that the first impact and dimple formation happens in about 5 ms while the slow drainage process takes more than 200 ms. Any attempt to describe this process using a full CFD simulation instead of a lubrication model has to be able to capture the details of the complex drainage phenomenon.

The pressure profiles are plotted in Fig. 8 for the same time instants as those of Fig. 6. The curvature inversion, a result of the pressure in the film exceeding the internal pressure, also called the Laplace pressure, $(2\sigma/R)$ of the bubble, occurs when $p > 374$ Pa and 228 Pa for $R = 385\ \mu m$ and 630 μm, respectively. During bubble approach the pressure is positive and is responsible for the deformation of the bubble. When the bubble starts to retreat, the pressure at the rim region becomes negative while the pressure at the centre is still positive.

In Fig. 9 we present the maximum radial water velocity as a function of radial position for the same time steps of Fig. 6. The maximum outward velocity is reached before the first shown profile appears; the velocity decreases as the film becomes

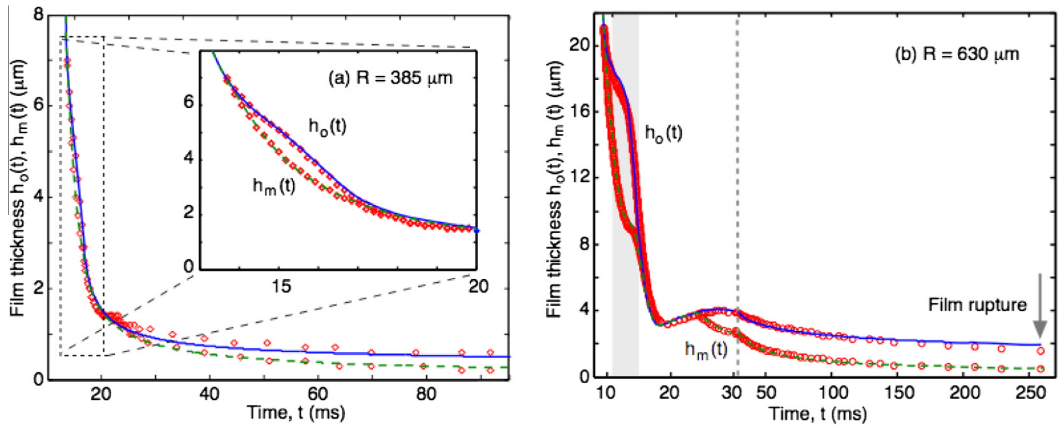

Fig. 7. Evolution of the position at the centre $h_o(t)$ and at the rim $h_m(t)$ of the dimple during first contact and subsequent film drainage for bubble having radius (a) 385 μm and (b) 630 μm. Symbols correspond to the experimental data while lubrication theory is plotted for $h_o(t)$ (dashed line) and for $h_m(t)$ (solid line).

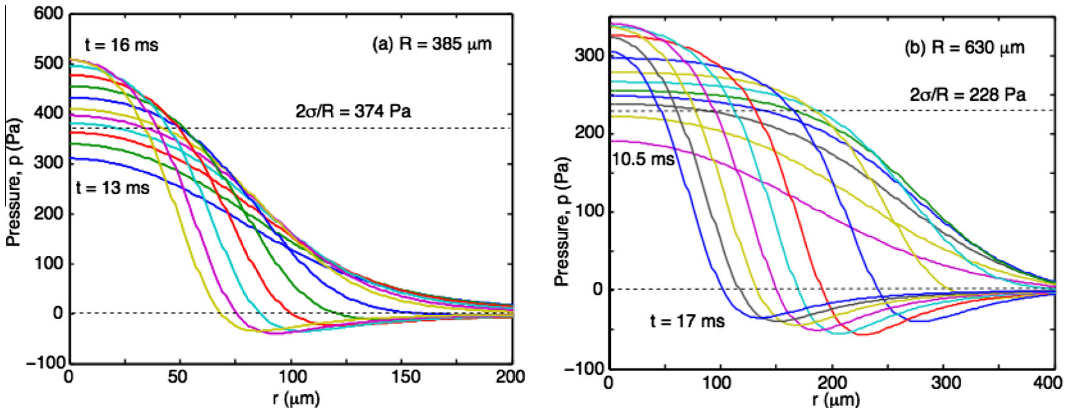

Fig. 8. Pressure profiles corresponding to the same time instants as in Fig. 6: (a) $R = 385$ μm and (b) $R = 630$ μm.

thinner. When the back of the bubble reverses from approach to retract the water has to occupy that space so that the velocity reverses from an outflow (positive) to an inflow (negative). On the other hand, the central part of the bubble continues to thin during this time.

In Fig. 10 we present shear stress calculated on the bubble surface (see Eq. (14)) for the same time instants shown in Fig. 6. It is interesting to note that the maximum shear stress occurs at the rim of the dimple and it changes sign when the bubble surface starts to separate from the glass plate. The magnitude of the shear stress is relatively small compared to that expected for a non-deforming sphere approaching the glass plate at the terminal velocity, V_T. The ability of the bubble interface to deform as it approaches the glass plate means that the rate of change of film thickness, dh/dt can become much smaller than V_T, and this then lowers the magnitude of the shear stress.

For comparison, we also show the variation of shear stress around the leading surface of a spherical bubble rising at the terminal velocity according to the CFD calculation using ANSYS Fluent (dashed line in Fig. 10(a)). We note that the shear stress on the deformed bubble surface as it interacts with the glass surface exceeds that at the leading part of a spherical bubble travelling at the terminal velocity with the tangentially immobile boundary condition.

In Fig. 11 we compare the maximum outward and inward radial water velocity as well as shear stresses as a function of time for the two cases analysed. Initially, during bubble approach, the water flows radially out of the film but eventually part of the flow will be radially inwards as the bubble starts to retreat from the glass surface. This means there is a circular position in the film where the velocity of the liquid is zero. The water velocity for the larger bubble is higher than that of the smaller one. On the other hand the shear stress is similar for both cases. Eventually the velocity and shear stress decrease as the bubble settles near the glass surface. The reason for the sudden change at around $t = 20$ ms comes from the fact the maximum shear stress changes position on the bubble surface.

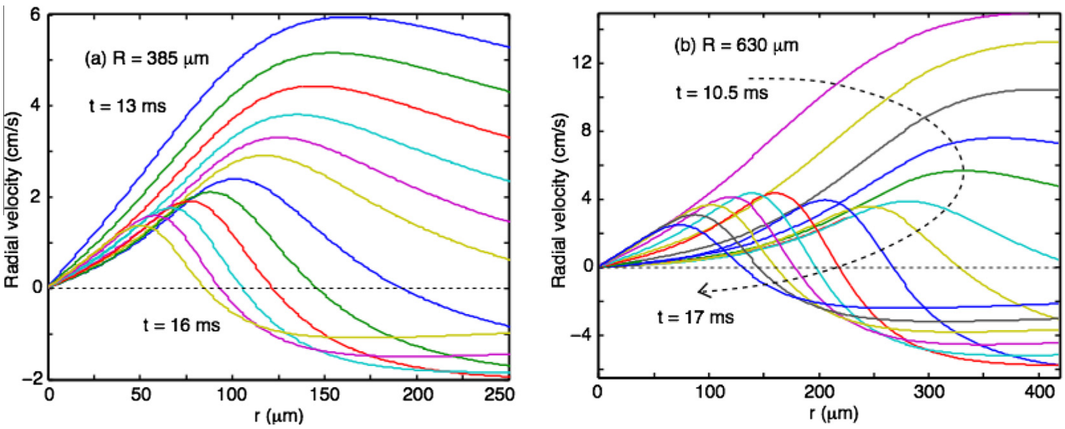

Fig. 9. Maximum radial velocity of the water inside the film calculated from Eq. (13) in the intervals corresponding to Fig. 6.

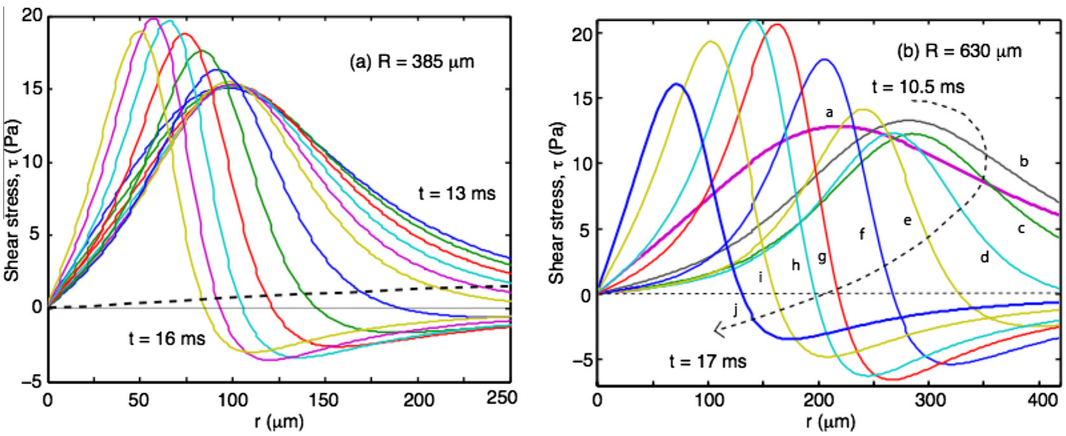

Fig. 10. Shear stress curves for the same time instants as those of Fig. 6 for bubbles of radius (a) 385 μm, (b) 630 μm. The dashed line in (a) corresponds to shear stress calculated from CFD simulations during bubble rise. Letters are added to the plot to guide the eye.

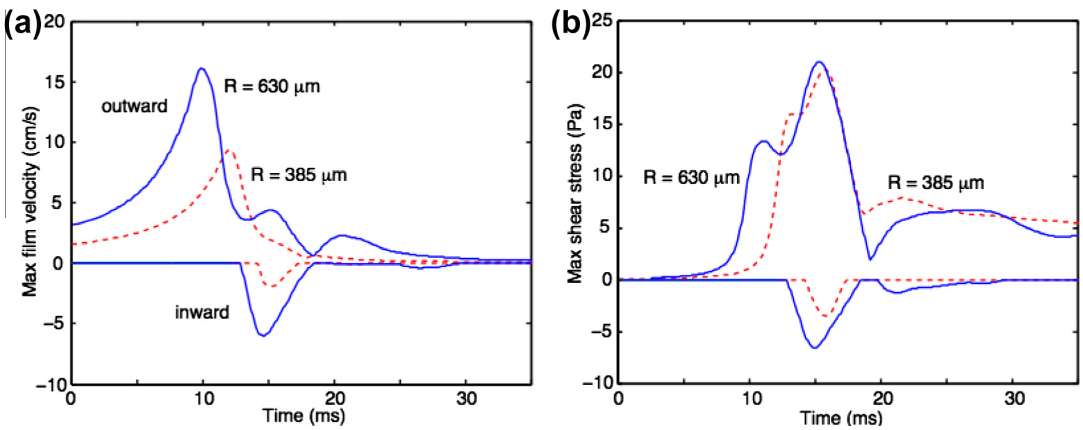

Fig. 11. (a) Maximum water velocity in the film as a function of time extracted from Fig. 9. Positive velocity means outward flow while negative velocity indicates that the water moves towards the centre. (b) Maximum (positive) and minimum (negative) shear stress at the bubble surface extracted from Fig. 10.

6. Discussion and conclusions

The technique applied in this work can be extended to other systems where different length scales appear, for example droplets falling on surfaces, coalescence of bubbles and drops. The combination of macro and micro scale modelling presented in this work allowed us to readily estimate quantities such as pressure profiles, fluid drainage velocities and shear stresses that are not yet captured experimentally. In these experiments, the bubble rise follows a linear trajectory and both deformation and film drainage happen with axial symmetry. Experiments for larger bubbles present helical or zigzag path during rise [38,39] and require more detailed modelling and numerical simulations to understand the intriguing physics involved.

Our direct observations show that the collision of a rising bubble with a flat solid surface involves phenomenon on rather different length scales. The velocity field due to the rising bubble varies on the scale of the bubble size (mm scale in the present experiments). However, the radial extent of the deformation of the bubble during collusion with the glass surface extends over $\sim$100–200 μm. The thickness of the water film deforms and thins on the scale of 1–10 μm until the film ruptures. Therefore in order to be able to have accurate resolution of all physical phenomena that spans such different lengths scales presents considerable challenge in a direct CFD simulation especially when bubble deformation is taken into account [40–42]. The need to resolve the shape of the bubble surface and the thin water film between the bubble and the solid surface would require highly refined grids that would increase considerably the computational time. Similar challenges are also found in the flow of Taylor bubbles [43,44] or drops [45] in channels, where the film separating the disperse phase from the tube wall can become thin.

The approach we have taken exploits the fact that the film deformation and drainage phenomena are characterised by the film Reynolds number, Re_f that remains small compared to unity. This permits the use of a low Reynolds number lubrication model to describe the dynamics of the water film trapped between the bubble and the solid surface together with (high Reynolds number) experimental velocity data that characterises bubble motion outside the film. This hybrid model captured the physics of the problem and provided accurate quantitative agreement with experiments.

Furthermore, our model predictions show that even as the bubble is retreating from the glass surface, the film is still draining and the local interface is approaching the glass surface until it eventually bounces, a result observed experimentally. This complex phenomenon was attributed to cause coalescence of drops when they were being separated in microfluidic channels [46,47] and also during the coalescence of two drops in a 4-roll mill experiment [48–50]. This phenomenon has also been observed in the coalescence of water bubbles [51] and drops [52] and also for mercury drops being separated from a surface [53]. Analytical attempts have been made to explain the experimental results [54] and also using the Hele-Shaw cell [55,56].

The tangentially immobile boundary condition that holds at the bubble surface is attributed to the presence of low concentration of surface-active impurities in the water that are capable of sustaining a small shear stress in the film. Earlier studies on the rise of bubbles in pure water [32] obtained terminal velocities of over 35 cm/s and those results were also confirmed by numerical solutions using mobile interfaces [33]. In our current experimental results, the bubbles attained velocities, which are less than half that value of about 15 cm/s for bubbles of the same size and compare well to experimental observations with small amount of known surfactant [4]. Recent work on the rise and film drainage show the possibility of mobile film drainage even when the bubble rise is immobile [17].

Appendix A. Derivation of the lubrication equations

The shape of the bubble close to the surface can be approximated as

$$h(r,T_o) = H_o + \frac{r^2}{2R} = H_o\left(1 + \frac{r^2}{2H_oR}\right), \tag{A1}$$

where H_o is a typical length scale, $T_o \sim H_o/V_o$ is a typical time scale and V_o is a typical vertical velocity scale. So the natural length scale for the radial coordinate r is $\sqrt{H_o\, R}$. In fact, using R as the radial length scale yields the same conclusions. We define the following scaled variables

$$\begin{aligned} u &= U_o\,\tilde{u},\\ v &= V_o\,\tilde{v},\\ t &= T_o\,\tilde{t},\\ r &= \sqrt{H_oR}\,\tilde{r},\\ z &= H_o\,\tilde{z},\\ p &= P_o\tilde{p}, \end{aligned} \tag{A2}$$

where U_o is a typical radial velocity scale and $P_o \sim \mu R V_o/H_o^2$ Introducing these scales into the continuity equation yields

$$\frac{U_o}{\sqrt{H_oR}}\,\frac{1}{\tilde{r}}\,\frac{\partial}{\partial\,\tilde{r}}(\tilde{r}\tilde{u}) + \frac{V_o}{H_o}\,\frac{\partial\tilde{v}}{\partial\tilde{z}} = 0, \tag{A3}$$

which implies

$$U_o \sim \sqrt{\frac{R}{H_o}} V_o. \tag{A4}$$

Introducing these scales in the Navier–Stokes equations (4) and (5) we obtain

$$\rho \frac{V_o}{T_o}\sqrt{\frac{R}{H_o}}\frac{\partial \tilde{u}}{\partial \tilde{t}} + \rho V_o^2 \frac{\sqrt{R}}{H_o^{3/2}}\tilde{u}\frac{\partial \tilde{u}}{\partial \tilde{r}} + \rho V_o^2 \frac{\sqrt{R}}{H_o^{3/2}}\tilde{v}\frac{\partial \tilde{u}}{\partial \tilde{z}} = -\frac{P_o}{\sqrt{H_o R}}\frac{\partial \tilde{p}}{\partial \tilde{r}} + \mu \frac{V_o}{R^{1/2}H^{3/2}}\frac{1}{\tilde{r}}\frac{\partial}{\partial r}\left[\tilde{r}\frac{\partial \tilde{u}}{\partial \tilde{r}}\right] + \mu V_o \frac{\sqrt{R}}{H_o^{5/2}}\frac{\partial^2 \tilde{u}}{\partial \tilde{z}^2} - \mu \frac{V_o}{R^{1/2}H_o^{3/2}}\frac{\tilde{u}}{\tilde{r}^2}, \tag{A5}$$

$$\rho \frac{V_o}{T_o}\frac{\partial \tilde{v}}{\partial \tilde{t}} + \rho \frac{V_o^2}{H_o}\tilde{u}\frac{\partial \tilde{v}}{\partial \tilde{r}} + \rho \frac{V_o^2}{H_o}\tilde{v}\frac{\partial \tilde{v}}{\partial \tilde{z}} = -\frac{P_o}{H_o}\frac{\partial \tilde{p}}{\partial \tilde{z}} + \mu \frac{V_o}{H_o R}\frac{1}{\tilde{r}}\frac{\partial}{\partial \tilde{r}}\left[\tilde{r}\frac{\partial \tilde{v}}{\partial \tilde{r}}\right] + \mu \frac{V_o}{H_o^2}\frac{\partial^2 \tilde{v}}{\partial \tilde{z}^2} \tag{A6}$$

and the film Reynolds number Re_f can be defined as

$$\mathrm{Re}_f = \frac{\rho H_o V_o}{\mu}. \tag{A7}$$

Introducing Re_f back into the NS equations yield

$$\mathrm{Re}_f\left(\frac{\partial \tilde{u}}{\partial \tilde{t}} + \tilde{u}\frac{\partial \tilde{u}}{\partial \tilde{r}} + \tilde{v}\frac{\partial \tilde{u}}{\partial \tilde{z}}\right) = -\frac{P_o H_o^2}{\mu V_o R}\frac{\partial \tilde{p}}{\partial \tilde{r}} + \frac{H_o}{R}\frac{1}{\tilde{r}}\frac{\partial}{\partial r}\left[\tilde{r}\frac{\partial \tilde{u}}{\partial \tilde{r}}\right] + \frac{\partial^2 \tilde{u}}{\partial \tilde{z}^2} - \frac{H_o}{R}\frac{\tilde{u}}{\tilde{r}^2}, \tag{A8}$$

$$\mathrm{Re}_f\left(\frac{\partial \tilde{v}}{\partial \tilde{t}} + \tilde{u}\frac{\partial \tilde{v}}{\partial \tilde{r}} + \tilde{v}\frac{\partial \tilde{v}}{\partial \tilde{z}}\right) = -\frac{P_o H_o}{\mu V_o}\frac{\partial \tilde{p}}{\partial \tilde{z}} + \frac{H_o}{R}\frac{1}{\tilde{r}}\frac{\partial}{\partial \tilde{r}}\left[\tilde{r}\frac{\partial \tilde{v}}{\partial \tilde{r}}\right] + \frac{\partial^2 \tilde{v}}{\partial \tilde{z}^2}. \tag{A9}$$

By discarding terms that are negligible, the lubrication equations (9)–(11) are obtained.

References

[1] R. Clift, J.R. Grace, M.E. Weber, Bubbles, Drops and Particles, Academic Press, NY, 1978.
[2] G.H. Kelsall, S. Tang, A.L. Smith, S. Yurdakul, Electrophoretic behaviour of bubbles in aqueous electrolytes, Faraday Trans. 92 (1996) 3879–3893.
[3] R. Bel Fdhila, P.C. Duineveld, The effect of surfactant on the rise of a spherical bubble at high Reynolds and Peclet numbers, Phys. Fluids 8 (1996) 310–321.
[4] K. Malysa, M. Krasowska, M. Krzan, Influence of surface active substances on bubble motion and collision with various interfaces, Adv. Colloid Interface Sci. 114–115 (2005) 205–225.
[5] V.G. Levich, Physicochemical Hydrodynamics, Prentice-Hall, Englewood Cliffs, NJ, 1962.
[6] B. Cuenot, J. Magnaudet, B. Spennato, The effects of slightly soluble surfactants on the flow around a spherical bubble, J. Fluid Mech. 339 (1997) 25–53.
[7] S.S. Sadhal, R.E. Johnson, Stokes flow past bubbles and drops partially covered with thin films. Part I: Stagnant cap of surfactant film – exact solution, J. Fluid Mech. 126 (1983) 237–250.
[8] H.-K. Tsao, D.L. Koch, Observations of high Reynolds number bubbles interacting with a rigid wall, Phys. Fluids 9 (1997) 44–56.
[9] R. Zenit, D. Legendre, The coefficient of restitution for air bubbles colliding against solid walls in viscous liquids, Phys. Fluids 21 (2009) 083306.
[10] F. Suñol, R. González-Cinca, Rise, bouncing and coalescence of bubbles impacting at a free surface, Colloids Surf. A: Physicochem. Eng. Asp. 365 (2010) 36–42.
[11] D. Kosior, J. Zawala, M. Krasowska, K. Malysa, Influence of n-octanol and α-terpineol on thin film stability and bubble attachment to hydrophobic surface, Phys. Chem. Chem. Phys. 15 (2013) 2586–2595.
[12] B.V. Derjaguin, M. Kussakov, Anomalous properties of thin polymolecular films, Acta Physicochim. URSS 10 (1939) 26–45 (Reprinted in Prog. Surf. Sci. 40 (1992) 26–45).
[13] L.R. Fisher, D. Hewitt, E.E. Mitchell, J. Ralston, J. Wolfe, The drainage of an aqueous film between a solid plane and an air bubble, Adv. Colloid Interface Sci. 39 (1992) 397–416.
[14] R. Manica, L. Parkinson, J. Ralston, D.Y.C. Chan, Interpreting the dynamic interaction between a very small rising bubble and a hydrophilic titania surface, J. Phys. Chem. C 114 (2010) 1942–1946.
[15] L. Parkinson, J. Ralston, Dynamic aspects of small bubble and hydrophilic solid encounters, Adv. Colloid Interface Sci. 168 (2011) 198–209.
[16] M.H.W. Hendrix, R. Manica, E. Klaseboer, D.Y.C. Chan, C.-D. Ohl, Spatiotemporal evolution of thin liquid films during impact of water bubbles on glass on a micrometer to nanometer scale, Phys. Rev. Lett. 108 (2012) 247803.
[17] R. Manica, M.H.W. Hendrix, E. Klaseboer, C.-D. Ohl, D.Y.C. Chan, Effect of film hydrodynamic boundary condition on bubble-wall impact, Soft Matter 9 (2013) 9755–9758.
[18] W. Bouwhuis, R.C.A. van der Veen, T. Tran, D.L. Keij, K.G. Winkels, I.R. Peters, D. van der Meer, C. Sun, J.H. Snoeijer, D. Lohse, Maximal air bubble entrainment at liquid-drop impact, Phys. Rev. Lett. 109 (2012) 264501.
[19] J.M. Kolinski, S.M. Rubinstein, S. Mandre, M.P. Brenner, D.A. Weitz, L. Mahadevan, Skating on a film of air: drops impacting on a surface, Phys. Rev. Lett. 108 (2012) 074503.
[20] J. Ruiter, J.M. Oh, D. van den Ende, F. Mugele, Dynamics of collapse of air films in drop impact, Phys. Rev. Lett. 108 (2012) 074505.
[21] T. Tran, H.J.J. Staat, A. Prosperetti, C. Sun, D. Lohse, Drop impact on superheated surfaces, Phys. Rev. Lett. 108 (2012) 036101.
[22] D. Quéré, Leidenfrost dynamics, Annu. Rev. Fluid Mech. 45 (2013) 197–215.
[23] F. Vincent, A. Le Goff, G. Lagubeau, D. Quéré, Bouncing bubbles, J. Adhes. 83 (2007) 897–906.
[24] J. Magnaudet, M. Rivero, J. Fabre, Accelerated flows past a rigid sphere or a spherical bubble. Part I. Pure straining flow, J. Fluid Mech. 284 (1995) 97–135.
[25] I. Nakamura, Steady wake behind a sphere, Phys. Fluids 19 (1976) 5–8.
[26] D.A. Jones, D.B. Clarke, Simulation of flow past a sphere using the Fluent code, Technical Report, Maritime Platforms Division, Australia, 2008.
[27] P.C. Duineveld, The rise velocity and shape of bubbles in pure water at high Reynolds number, J. Fluid Mech. 292 (1995) 325–332.

[28] E. Klaseboer, R. Manica, D.Y.C. Chan, B.C. Khoo, BEM simulations of potential flow with viscous effects as applied to a rising bubble, Eng. Anal. Bound. Elem. 35 (2011) 489–494.
[29] D.W. Moore, The boundary layer on a spherical gas bubble, J. Fluid Mech. 16 (1963) 161–176.
[30] D.W. Moore, The velocity of rise of distorted gas bubbles in a liquid of small viscosity, J. Fluid Mech. 23 (1965) 749–766.
[31] E. Klaseboer, J.-P.h. Chevaillier, C. Gourdon, O. Masbernat, Film drainage between colliding drops at constant approach velocity: experiments and modeling, J. Colloid Interface Sci. 229 (2000) 274–285.
[32] D.Y.C. Chan, E. Klaseboer, R. Manica, Film drainage and coalescence between deformable drops and bubbles, Soft Matter 7 (2010) 2235–2264.
[33] D.Y.C. Chan, E. Klaseboer, R. Manica, Theory of non-equilibrium force measurements involving deformable drops and bubbles, Adv. Colloid Interface Sci. 165 (2011) 70–90.
[34] S.G. Yiantsios, R.H. Davis, On the buoyancy-driven motion of a drop towards a rigid surface or a deformable interface, J. Fluid Mech. 217 (1990) 547–573.
[35] E. Klaseboer, J.-P.h. Chevaillier, A. Maté, O. Masbernat, C. Gourdon, Model and experiments of a drop impinging on an immersed wall, Phys. Fluids 13 (2001) 45–57.
[36] K. Kamran, S.L. Carnie, Modeling the gentle bouncing of a drop with quasi-static thin film equations, Chem. Eng. Sci. 104 (2013) 361–373.
[37] I.U. Vakarelski, R. Manica, X. Tang, S.J. O'Shea, G.W. Stevens, F. Grieser, R.R. Dagastine, D.Y.C. Chan, Dynamic interactions between microbubbles in water, Proc. Nat. Acad. Sci. 107 (2010) 11177–11182.
[38] J. Magnaudet, I. Eames, The motion of high-Reynolds-number bubbles in inhomogeneous flows, Annu. Rev. Fluid Mech. 32 (2000) 659–708.
[39] A.W.G. De Vries, A. Biesheuvel, L. van Wijngaarden, Notes on the path and wake of a gas bubble rising in pure water, Int. J. Multiphase Flow 28 (2002) 1823–1835.
[40] A. Smolianski, H. Haario, P. Luukka, Vortex shedding behind a rising bubble and two-bubble coalescence. A numerical approach, Appl. Math. Model. 29 (2005) 615–632.
[41] A. Smolianski, H. Haario, P. Luukka, Numerical study of dynamics of single bubbles and bubble swarms, Appl. Math. Model. 32 (2008) 641–659.
[42] J. Hua, J. Lou, Numerical simulation of bubble rising in viscous liquid, J. Comput. Phys. 222 (2007) 769–795.
[43] R. Gupta, D.F. Fletcher, B.S. Haynes, Taylor flow in microchannels: a review of experimental and computational work, J. Comput. Multiphase Flows 2 (2010) 1–31.
[44] A.N. Asadolahi, R. Gupta, S.S.Y. Leung, D.F. Fletcher, B.S. Haynes, Validation of a CFD model of Taylor flow hydrodynamics and heat transfer, Chem. Eng. Sci. 69 (2012) 541–552.
[45] R. Gupta, S.S.Y. Leung, R. Manica, D.F. Fletcher, B.S. Haynes, Hydrodynamics of liquid–liquid Taylor flow in microchannels, Chem. Eng. Sci. 92 (2013) 180–189.
[46] N. Bremond, A.R. Thiam, J. Bibette, Decompressing emulsion droplets favors coalescence, Phys. Rev. Lett. 100 (2008) 024501.
[47] D.Z. Gunes, X. Clain, O. Breton, G. Mayor, A.S. Burbidge, Avalanches of coalescence events and local extensional flows – stabilisation or destabilisation due to surfactant, J. Colloid Interface Sci. 343 (2010) 79–86.
[48] Y. Yoon, F. Baldessari, H.D. Ceniceros, L.G. Leal, Coalescence of two equal-sized deformable drops in an axisymmetric flow, Phys. Fluids 19 (2007) 102102.
[49] C. Vannozzi, Relaxation and coalescence of two equal-sized viscous drops in a quiescent matrix, J. Fluid Mech. 694 (2012) 408–425.
[50] C. Vannozzi, Coalescence of surfactant covered drops in extensional flows: effects of the interfacial diffusivity, Phys. Fluids 24 (2012) 082101.
[51] F.H. Zhang, S.T. Thoroddsen, Satellite generation during bubble coalescence, Phys. Fluids 20 (2008) 022104.
[52] F.H. Zhang, E.Q. Li, S.T. Thoroddsen, Satellite formation during coalescence of unequal size drops, Phys. Rev. Lett. 102 (2009) 104502.
[53] R. Manica, J.N. Connor, L.Y. Clasohm, S.L. Carnie, R.G. Horn, D.Y.C. Chan, Transient responses of a wetting film to mechanical and electrical perturbations, Langmuir 24 (2008) 1381–1390.
[54] D.Y.C. Chan, E. Klaseboer, R. Manica, Dynamic deformations and forces in soft matter, Soft Matter 5 (2009) 2858–2861.
[55] A. Lai, N. Bremond, H.A. Stone, Separation-driven coalescence of droplets: an analytical criterion for the approach to contact, J. Fluid Mech. 632 (2009) 97–107.
[56] D.Y.C. Chan, E. Klaseboer, R. Manica, Dynamic interactions between deformable drops in the Hele–Shaw geometry, Soft Matter 6 (2010) 1809–1815.